1-2020

Stochastic Complex Transmittance Screens for Synthesizing General Partially Coherent Sources

Milo W. Hyde IV
Air Force Institute of Technology

Stochastic complex transmittance screens for synthesizing general partially coherent sources

MILO W. HYDE ®

Air Force Institute of Technology, Dayton, Ohio 45433, USA (milo.hyde@us.af.mil)

We develop a method to synthesize any partially coherent source (PCS) with a genuine cross-spectral density (CSD) function using complex transmittance screens. Prior work concerning PCS synthesis with complex transmittance screens has focused on generating Schell-model (uniformly correlated) sources. Here, using the necessary and sufficient condition for a genuine CSD function, we derive an expression, in the form of a superposition integral, that produces stochastic complex screen realizations. The sample autocorrelation of the screens is equal to the complex correlation function of the desired PCS. We validate our work by generating, in simulation, three PCSs from the literature—none has ever been synthesized using stochastic screens before. Examining planar slices through the four-dimensional CSD functions, we find the simulated results to be in excellent agreement with theory, implying successful realization of all three PCSs. The technique presented herein adds to the existing literature concerning the generation of PCSs and can be physically implemented using a simple optical setup consisting of a laser, spatial light modulator, and spatial filter.

1. INTRODUCTION

Generating partially coherent sources (PCSs) has been an active area of research for the past two decades. This research is motivated by the plethora of applications in which control over spatial coherence is advantageous. These include, but are not limited to, free-space/underwater optical communications, optical trapping, medicine, and remote sensing [1–5]. A survey of the literature reveals three main PCS synthesis techniques: Van Cittert–Zernike theorem (VCZT), coherent modes or pseudo-modes, and complex transmittance screen or phase screen methods.

VCZT-based techniques generally involve propagating a quasihomogeneous PCS [5,6] through a linear optical system, where the desired PCS is produced at the output. The details of the individual optical systems vary; however, all generally rely on the Fourier transforming properties of spherical lenses and the generalized VCZT [6,7] to produce the desired source [3,4,8–14].

The primary benefit of VCZT approaches, vice the other two, is that the desired PCS is generated in near real time, as the quasihomogeneous PCS fed into the optical system is typically a spatially incoherent source, e.g., a thermal source, light emitting diode, or multimode fiber fed by a temporally incoherent (broadband) light source [15–19]. While not theoretically limited, VCZT techniques are practically restricted to producing only Schell-model (uniformly correlated) sources, which can be synthesized using paraxial, shift-invariant (or isoplanatic)

optical systems. To synthesize non-uniformly correlated PCSs, the corresponding optical systems must be anisoplanatic, which are very difficult to design and build.

Coherent mode approaches rely on the coherent mode decomposition [5,6] of the PCS. Using a laser and a spatial light modulator (SLM), each mode of the expansion is synthesized with the proper weight and summed incoherently at the detector [20–22]. This approach can produce any PCS (uniformly or non-uniformly correlated) for which the coherent modes representation is known. Unfortunately, there are relatively few.

For PCSs with unknown coherent mode decompositions, pseudo-modes can be used [23–29]. In contrast with coherent modes, pseudo-modes are generally not orthogonal and therefore require more modes to accurately synthesize the PCS. We last note that since the coherent modes or pseudo-modes are generated serially, these approaches require time averaging.

Complex transmittance screen or phase screen methods (hereafter referred to as complex screen methods) generate stochastic screens with the proper spatial statistics by filtering circular complex Gaussian random numbers (CCGRNs) [5,30–37]. These screens are then commanded to a SLM, which, in combination with a laser, produces a stochastic field realization (a realization drawn from the statistical ensemble) of the desired PCS.

Similar to coherent mode approaches, complex screen PCSs are formed from the incoherent sum of many statistically independent stochastic field realizations and therefore require time averaging. On the other hand, unlike coherent mode

approaches, complex screen methods produce PCS field realizations with thermal or pseudo-thermal light statistics [7] (useful in some applications) and can easily (relatively speaking) be generalized to produce electromagnetic PCSs [34,38]—qualities shared with VCZT methods.

Like VCZT techniques, complex screen methods have been used to generate only Schell-model sources. For Schell-model sources, the filters—used to "color" the "white" CCGRNs—are shift invariant, and the filtering operation simplifies to convolution, which can be efficiently performed using the convolution theorem and fast Fourier transforms (FFTs).

In a few instances, complex screens have been used to synthesize non-uniformly correlated sources [34,39,40]. In Ref. [34], the authors used Cholesky factorization [41] to produce non-uniformly correlated screens—a computationally intensive procedure in terms of both memory and processing power. In Refs. [39,40], the authors generated non-uniformly correlated screens by nonlinearly transforming Gaussian Schell-model [5,6] screens.

Here, we extend the existing PCS synthesis literature by demonstrating how to synthesize general PCSs with complex screens. In the next section, using the genuine cross-spectral density (CSD) function criterion [42], we derive a superposition integral to produce a complex screen realization. We then apply that integral to generate (in simulation) stochastic field realizations for three PCSs from the literature. Using these field realizations, we compute several planar cuts through the associated four-dimensional (4D) CSD functions and compare those results to theory. Last, we conclude with a brief summary.

Before proceeding, we do not claim that the generalized complex screen method presented herein is superior to the others summarized above. The question of which technique is superior ultimately depends on the application. For example, in free-space optical communications (FSOC) using PCSs, the rate at which the PCS produces statistically independent field realizations must be significantly larger than the communications modulation frequency. This ensures that the optical detector incoherently sums or integrates many independent field realizations per digital bit thereby reducing turbulence-induced scintillation and ultimately decreasing bit-error rate. Since FSOC data rates are gigabits to terabits per second, a VCZT method, with near real-time synthesis of the PCS, is the superior option [43,44].

Therefore, the purpose of this paper is twofold: (1) to generalize complex screen approaches to produce any PCS with a genuine CSD function and (2) to provide another option for generating PCSs, in particular, non-uniformly correlated PCSs, with a simple optical setup consisting of a laser, SLM, and $4f$ spatial filter.

2. THEORY

In the analysis to follow, we assume that the CSD function W can be expressed as

$$W(\boldsymbol{\rho}_1, \boldsymbol{\rho}_2) = \tau(\boldsymbol{\rho}_1) \tau^*(\boldsymbol{\rho}_2) \mu(\boldsymbol{\rho}_1, \boldsymbol{\rho}_2), \quad \text{(1)}$$

where $\boldsymbol{\rho} = \hat{\boldsymbol{x}}x + \hat{\boldsymbol{y}}y$, τ is, in general, a complex function and physically manifests as the source's shape, and μ is the complex correlation function [6].

We begin our analysis by recalling the necessary and sufficient condition for a genuine W:

$$W(\boldsymbol{\rho}_1, \boldsymbol{\rho}_2) = \iint_{-\infty}^{\infty} p(\boldsymbol{v}) H(\boldsymbol{\rho}_1, \boldsymbol{v}) H^*(\boldsymbol{\rho}_2, \boldsymbol{v}) \, \mathrm{d}^2 v, \quad \text{(2)}$$

where $\boldsymbol{v} = \hat{\boldsymbol{x}}v_x + \hat{\boldsymbol{y}}v_y$, p is a positive function, and H is an arbitrary kernel [23,42]. Here, we assume that H takes the form

$$H(\boldsymbol{\rho}, \boldsymbol{v}) = \tau(\boldsymbol{\rho}) h(\boldsymbol{\rho}, \boldsymbol{v}). \quad \text{(3)}$$

If we let H be a realization of an optical field parameterized by random vector $\boldsymbol{v}$, then taking the autocorrelation of Eq. (3), we recover Eq. (2), where p becomes the joint probability density function of $\boldsymbol{v} = (v_x, v_y)$ [24,26,27]. Comparing the resulting autocorrelation to Eq. (1), we see that the complex correlation function μ is

$$\mu(\boldsymbol{\rho}_1, \boldsymbol{\rho}_2) = \iint_{-\infty}^{\infty} p(\boldsymbol{v}) h(\boldsymbol{\rho}_1, \boldsymbol{v}) h^*(\boldsymbol{\rho}_2, \boldsymbol{v}) \, \mathrm{d}^2 v. \quad \text{(4)}$$

We now consider the form of a stochastic field generated by passing a deterministic beam through a random complex transmittance screen T, i.e.,

$$U(\boldsymbol{\rho}) = \tau(\boldsymbol{\rho}) T(\boldsymbol{\rho}), \quad \text{(5)}$$

where T is the complex screen generated from CCGRNs [32–34]. Taking the autocorrelation of Eq. (5) and comparing to Eq. (1) reveals

$$\mu(\boldsymbol{\rho}_1, \boldsymbol{\rho}_2) = \langle T(\boldsymbol{\rho}_1) T^*(\boldsymbol{\rho}_2) \rangle. \quad \text{(6)}$$

Equations (4) and (6) imply

$$\langle T(\boldsymbol{\rho}_1) T^*(\boldsymbol{\rho}_2) \rangle = \iint_{-\infty}^{\infty} p(\boldsymbol{v}) h(\boldsymbol{\rho}_1, \boldsymbol{v}) h^*(\boldsymbol{\rho}_2, \boldsymbol{v}) \, \mathrm{d}^2 v; \quad \text{(7)}$$

however, this expression provides little insight into how to generate T. To gain this insight, we briefly assume we are interested in generating Schell-model (uniformly correlated) sources [5–7].

For Schell-model sources, the kernel h in Eq. (3) is $h(\boldsymbol{\rho}, \boldsymbol{v}) = \exp(j\boldsymbol{v} \cdot \boldsymbol{\rho})$ [42], and

$$T(\boldsymbol{\rho}) = \iint_{-\infty}^{\infty} r(\boldsymbol{f}) \left[\frac{1}{2}\Phi(\boldsymbol{f})\right]^{1/2} \exp(j2\pi \boldsymbol{f} \cdot \boldsymbol{\rho}) \, \mathrm{d}^2 f, \quad \text{(8)}$$

where $\boldsymbol{f} = \hat{\boldsymbol{x}}f_x + \hat{\boldsymbol{y}}f_y$ is the spatial frequency vector, and r is a delta-correlated function composed of zero-mean, unit-variance, CCGRNs [32–34]. Also in Eq. (8), Φ is the source's spatial power spectrum and equal to

$$\Phi(\boldsymbol{f}) = \iint_{-\infty}^{\infty} \mu(\boldsymbol{\rho}_d) \exp(-j2\pi \boldsymbol{f} \cdot \boldsymbol{\rho}_d) \, \mathrm{d}^2 \rho_d, \quad \text{(9)}$$

where $\boldsymbol{\rho}_d = \boldsymbol{\rho}_1 - \boldsymbol{\rho}_2$. Substituting $h(\boldsymbol{\rho}, \boldsymbol{v}) = \exp(j\boldsymbol{v} \cdot \boldsymbol{\rho})$ into Eq. (7) and taking the autocorrelation of Eq. (8) produces

$$\iint_{-\infty}^{\infty} \Phi(\boldsymbol{f}) \exp(j2\pi \boldsymbol{f} \cdot \boldsymbol{\rho}_d) \, \mathrm{d}^2 f$$

$$= \iint_{-\infty}^{\infty} p(\boldsymbol{v}) \exp(j\boldsymbol{v} \cdot \boldsymbol{\rho}_d) \, \mathrm{d}^2 v. \quad \text{(10)}$$

To arrive at the left-hand side of Eq. (10), we use

$$\langle r\left(f_1\right) r^*\left(f_2\right)\rangle = \langle r^{\mathrm r}\left(f_1\right) r^{\mathrm r}\left(f_2\right)\rangle + \langle r^{\mathrm i}\left(f_1\right) r^{\mathrm i}\left(f_2\right)\rangle$$
$$+ \mathrm j\left[\langle r^{\mathrm i}\left(f_1\right) r^{\mathrm r}\left(f_2\right)\rangle - \langle r^{\mathrm r}\left(f_1\right) r^{\mathrm i}\left(f_2\right)\rangle\right]$$
$$= 2\delta\left(f_1 - f_2\right),$$

(11)

where superscripts "r" and "i" correspond to the real and imaginary parts, and δ is the Dirac delta function.

From Eq. (10), it is clear that Φ is proportional to p, and h (a Fourier kernel) gives rise to the Fourier kernel in Eq. (8). We can now generalize the Schell-model expression for T given in Eq. (8) to that of any PCS whose W can be expressed as Eq. (1):

$$T(\boldsymbol{\rho}) = \iint_{-\infty}^{\infty} r\left(f\right)\left[\frac{1}{2}(2\pi)^2 p\left(2\pi f\right)\right]^{1/2} h\left(\boldsymbol{\rho}, 2\pi f\right) \mathrm d^2 f,$$

(12)

where the $(2\pi)^2$ comes from enforcing the requirement that the volumes under both Φ and p be unity.

Note that Eq. (12) is equivalent to passing CCGRNs through a filter, whose impulse response h is shift variant. Computationally, this is equivalent to a matrix–vector product, and therefore requires $O(N^2)$ operations. This is an improvement over Cholesky decomposition, which requires an initial $O(N^3)$ operation to compute the Cholesky factor, and then $O(N^2)$ operations (a matrix–vector product) to generate T [34,41]. As we show in the next section, in many instances, we can take advantage of the form of h to evaluate the integrals in Eq. (12) more efficiently than computing the matrix–vector product, i.e., by reducing dimensionality (significantly reducing N), or by using FFTs [complexity $O(N\log N)$].

3. EXAMPLES

Here, we apply the theory in Section 2 to generate complex transmittance screens T for three PCSs from the literature. We simulate the generation of these beams and compare the simulated second-order statistical moments to their corresponding theoretical CSD expressions.

A. I_m-Bessel Correlated Beam

We begin with an I_m-Bessel correlated source, which was first introduced by Ponomarenko [45] in 2001 and only recently synthesized in Refs. [20,27]. The CSD function for an I_m-Bessel correlated source is

$$W\left(\boldsymbol{\rho}_1, \boldsymbol{\rho}_2\right) = \frac{\xi^{-m/2}}{1-\xi} \exp\left(-\frac{1+\xi}{1-\xi}\frac{\rho_1^2 + \rho_2^2}{\sigma^2}\right)$$
$$\times \exp\left[-\mathrm jm\left(\phi_1 - \phi_2\right)\right] I_m\left(\frac{4\sqrt{\xi}}{1-\xi}\frac{\rho_1\rho_2}{\sigma^2}\right),$$

(13)

where m is an integer and the topological charge of the vortex, I_m is an mth-order, first-kind, modified Bessel function, σ is the size of the source, and $0 < \xi < 1$ is a measure of the spatial

coherence of the field ($\xi \to 0$ is a coherent field; $\xi \to 1$ is an incoherent field) [5,20,27,45]. In Ref. [27], the author found that letting

$$\tau\left(\boldsymbol{\rho}\right) = \sqrt{\frac{\xi^{-m/2}}{1-\xi}} \exp\left(-\mathrm jm\phi\right) \exp\left[-\frac{\left(1-\sqrt{\xi}\right)^2}{1-\xi}\frac{\rho^2}{\sigma^2}\right],$$
$$p\left(\boldsymbol{v}\right) = \frac{1}{\pi}\frac{\sigma^2}{8}\frac{1-\xi}{\sqrt{\xi}} \exp\left(-\frac{\sigma^2}{8}\frac{1-\xi}{\sqrt{\xi}}v^2\right),$$
$$h\left(\boldsymbol{\rho}, \boldsymbol{v}\right) = J_m\left(\rho v\right),$$

(14)

where J_m is a mth-order Bessel function of the first kind, produced [via Eq. (2)] an I_m-Bessel correlated source.

With this, we can apply Eq. (12) to produce T, which, in combination with τ, yield stochastic I_m-Bessel correlated beam realizations. We note that since μ is rotationally invariant, T and subsequently r must be as well. Applying this to Eq. (12), transforming the integrals into polar coordinates, and evaluating the trivial integral over angle produces

$$T(\rho) = (2\pi)^{3/2}\sqrt{\frac{\sigma^2}{8}\frac{1-\xi}{\sqrt{\xi}}} \int_0^{\infty} fr\left(f\right)\exp$$
$$\times\left[-\frac{1}{2}(2\pi)^2\frac{\sigma^2}{8}\frac{1-\xi}{\sqrt{\xi}}f^2\right] J_m\left(2\pi\rho f\right)\mathrm df.$$

(15)

Taking the autocorrelation of T yields

$$\langle T(\rho_1) T^*(\rho_2)\rangle = (2\pi)^3\frac{\sigma^2}{8}\frac{1-\xi}{\sqrt{\xi}}\iint_0^{\infty} f_1 f_2\langle r(f_1)r^*(f_2)\rangle$$
$$\times\exp\left[-\frac{1}{2}(2\pi)^2\frac{\sigma^2}{8}\frac{1-\xi}{\sqrt{\xi}}\left(f_1^2 + f_2^2\right)\right]$$
$$\times J_m\left(2\pi\rho_1 f_1\right) J_m\left(2\pi\rho_2 f_2\right)\mathrm df_1\mathrm df_2.$$

(16)

The moment $\langle r(f_1)r^*(f_2)\rangle = \delta(f_1 - f_2)/(\pi f_1)$ for Eq. (16) to simplify to the desired μ. Subsequently, Eq. (16) becomes

$$\langle T(\rho_1) T^*(\rho_2)\rangle = \mu\left(\rho_1, \rho_2\right) = (2\pi)^3\frac{1}{\pi}\frac{\sigma^2}{8}\frac{1-\xi}{\sqrt{\xi}}$$
$$\times\int_0^{\infty} f\exp\left[-(2\pi)^2\frac{\sigma^2}{8}\frac{1-\xi}{\sqrt{\xi}}f^2\right]$$
$$\times J_m\left(2\pi\rho_1 f\right) J_m\left(2\pi\rho_2 f\right)\mathrm df.$$

(17)

Unfortunately, we cannot numerically generate CCGRNs with the above autocorrelation function because of the singularity at $f_1 = 0$. We can work around this difficulty by slightly modifying Eq. (15), such that

$$T(\rho) = (2\pi)^{3/2}\sqrt{\frac{\sigma^2}{8}\frac{1-\xi}{\sqrt{\xi}}} \int_0^{\infty} r\left(f\right)\sqrt{f}$$
$$\times\exp\left[-\frac{1}{2}(2\pi)^2\frac{\sigma^2}{8}\frac{1-\xi}{\sqrt{\xi}}f^2\right] J_m\left(2\pi\rho f\right)\mathrm df.$$
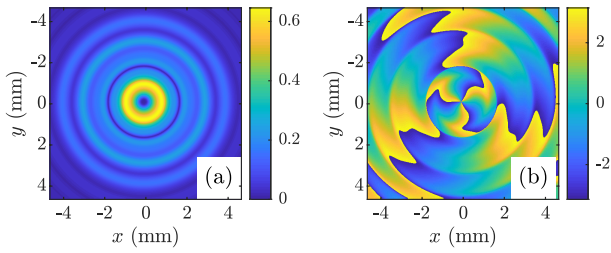
(18)

Fig. 1. I_m-Bessel correlated field realization: (a) $|U|$ and (b) $\arg(U)$.

The autocorrelation of the above expression equals Eq. (17) or equivalently μ, if $\langle r(f_1)r^*(f_2)\rangle = \delta(f_1 - f_2)/\pi$. CCGRNs with that autocorrelation function are easy to create with a Gaussian random number generator, and we can use Eq. (18) to produce T.

Because Eq. (18) will be computed numerically, we express it in discrete form:

$$T[i] = 2\pi \sqrt{\frac{\sigma^2}{8}\frac{1-\xi}{\sqrt{\xi}}} \sum_{n=0}^{N-1} r[n]\sqrt{n\Delta_f}$$

$$\times \exp\left[-\frac{1}{2}(2\pi)^2 \frac{\sigma^2}{8}\frac{1-\xi}{\sqrt{\xi}}\left(n\Delta_f\right)^2\right]$$

$$\times J_m\left(2\pi i n\Delta_s\Delta_f\right)\sqrt{\Delta_f}, \tag{19}$$

where r is a one-dimensional array of zero-mean, unit-variance CCGRNs, i is the discrete radial index, n is the discrete f index, Δ_s is the sample spacing in the spatial domain, Δ_f is the spacing in the f domain, and N is the number of discrete points in the array. Note that the integral (sum) is now one dimensional vice two, and therefore, it is not prohibitive to directly compute what is equivalently an mth-order Hankel transform. After computing Eq. (19), to produce an I_m-Bessel correlated beam realization, we need to transform the one-dimensional T into a two-dimensional (2D), rotationally invariant screen and then multiply the screen by τ given in Eq. (14).

Figure 1 shows an example I_m-Bessel correlated field realization generated using the above procedure. As we show in Code 1, Ref. [46], we used computational grids that were $N = 512$ points per side with $\Delta_s = 18.2$ μm and $\Delta_f = 107.4$ m^{-1}. The I_m-Bessel correlated source parameters were $\xi = 0.7$, $m = 3$, and $\sigma = 1$ mm.

Figure 2 shows the theoretical [computed using Eq. (13)] and simulated spectral densities $[S(\boldsymbol{\rho}) = W(\boldsymbol{\rho}, \boldsymbol{\rho})]$ [5,6] and $W(x_1, y_1, \gamma, \gamma)$, where γ is

$$\gamma = \sqrt{\frac{\sigma^2}{8}\frac{1-\xi}{\sqrt{\xi}}} = 211.7 \ \mu\text{m}. \tag{20}$$

The simulated moments were computed using 100,000 I_m-Bessel correlated field realizations. Figure 2(c) shows the 2D correlation coefficient C for the simulated spectral density versus trial number. The inset shows C from trials 100–100,000. This plot is included to quantitatively show convergence. The simulated results are in excellent agreement with theory.
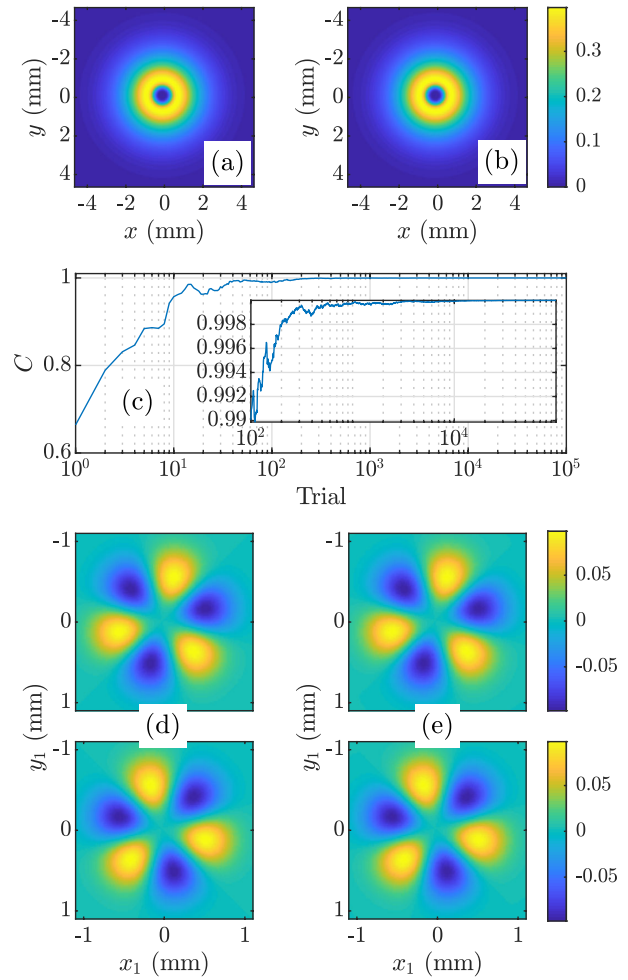

Fig. 2. I_m-Bessel correlated source simulation results: (a) S theory, (b) S simulation, (c) 2D correlation coefficient C for S simulation versus trial number, (d) real (top) and imaginary (bottom) parts of $W(x_1, y_1, \gamma, \gamma)$ theory, and (e) real (top) and imaginary (bottom) parts of $W(x_1, y_1, \gamma, \gamma)$ simulation.

B. Rectangular Hermite Non-Uniformly Correlated Source

We now show how to generate rectangular Hermite non-uniformly correlated (RHNUC) source field realizations. To our knowledge, RHNUC beams have never been synthesized before.

RHNUC beams were introduced in Ref. [47] and have the following W:

$$W(\boldsymbol{\rho}_1, \boldsymbol{\rho}_2) = \exp\left(-\frac{x_1^2 + x_2^2}{4\sigma_x^2}\right)\frac{1}{H_{2m}(0)}H_{2m}\left[\frac{f(x_1, x_2)}{\delta_x^2}\right]$$

$$\times \exp\left[-\frac{f^2(x_1, x_2)}{\delta_x^4}\right]\exp\left(-\frac{y_1^2 + y_2^2}{4\sigma_y^2}\right)$$

$$\times \frac{1}{H_{2n}(0)}H_{2n}\left[\frac{g(y_1, y_2)}{\delta_y^2}\right]\exp\left[-\frac{g^2(y_1, y_2)}{\delta_y^4}\right], \tag{21}$$

where m and n are integers, H_{2m} is a $2m$th-order Hermite polynomial, σ_x and σ_y are the radii of the beam in the x and y directions, and δ_x and δ_y are related to the correlation widths in the x and y directions, respectively. Also in Eq. (21), f and g are

$$f(x_1, x_2) = (x_1 - x_0)^2 - (x_2 - x_0)^2,$$

$$g(y_1, y_2) = (y_1 - y_0)^2 - (y_2 - y_0)^2, \qquad \textbf{(22)}$$

where x_0 and y_0 are shift parameters in the x and y directions. The τ, p, and h that when substituted into Eq. (2) yield the RHNUC source W are

$$\tau(\boldsymbol{\rho}) = \exp\left(-\frac{x^2}{4\sigma_x^2}\right)\exp\left(-\frac{y^2}{4\sigma_y^2}\right),$$

$$p(\boldsymbol{v}) = \frac{(\delta_x^4/4)^{m+1/2}(\delta_y^4/4)^{n+1/2}}{\Gamma(m+1/2)\,\Gamma(n+1/2)}v_x^{2m}v_y^{2n}$$
$$\times \exp\left(-\frac{\delta_x^4}{4}v_x^2\right)\exp\left(-\frac{\delta_y^4}{4}v_y^2\right),$$

$$h(\boldsymbol{\rho},\boldsymbol{v}) = \exp\left[-jv_x(x-x_0)^2\right]\exp\left[-jv_y(y-y_0)^2\right], \quad \textbf{(23)}$$

where Γ is the gamma function.

We can now apply Eq. (12) to generate T and ultimately a RHNUC source field realization. Substituting the above p and h into Eq. (12) and simplifying yields

$$T(\boldsymbol{\rho}) = \frac{(\delta_x/\sqrt{2})^{2m+1}(\delta_y/\sqrt{2})^{2n+1}}{\sqrt{2}\Gamma(m+1/2)\,\Gamma(n+1/2)}(2m)^{m+1/2}(2n)^{n+1/2}$$
$$\times \iint_{-\infty}^{\infty} r(\boldsymbol{f})\,|f_x|^m|f_y|^n\exp\left(-\frac{1}{2}\pi^2\delta_x^4 f_x^2\right)$$
$$\times \exp\left(-\frac{1}{2}\pi^2\delta_y^4 f_y^2\right)\exp\left[-j2\pi f_x(x-x_0)^2\right]$$
$$\times \exp\left[-j2\pi f_y(y-y_0)^2\right]\mathrm{d}f_x\mathrm{d}f_y.$$
$$\textbf{(24)}$$

The integrals in Eq. (24) can be evaluated using FFTs. The transform domain coordinates, ξ and η, are related to the spatial domain coordinates, x and y, by

$$\xi = (x - x_0)^2,$$

$$\eta = (y - y_0)^2. \qquad \textbf{(25)}$$

Assuming square computational grids, the grid size in the (ξ, η) plane is

$$L_{\xi\eta} = 2\left[\frac{L_{xy}}{\sqrt{2}} + \max(|x_0|, |y_0|)\right]^2, \qquad \textbf{(26)}$$

where L_{xy} is the grid size in the (x, y) plane, which must be large enough to comfortably "fit" the beam shape τ. Equation (24) in 2D discrete Fourier transform (DFT) form is
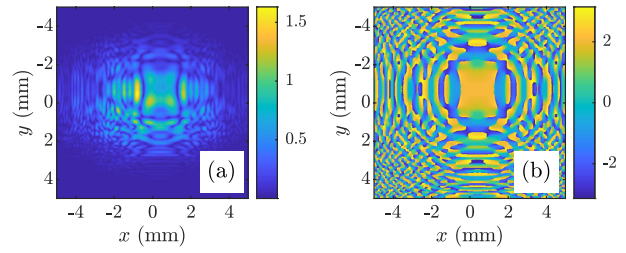

Fig. 3. RHNUC field realization: (a) $|U|$ and (b) $\arg(U)$.

$$T[i, j] = \frac{(\delta_x/\sqrt{2})^{2m+1}(\delta_y/\sqrt{2})^{2n+1}}{\sqrt{2}\Gamma(m+1/2)\,\Gamma(n+1/2)}(2m)^{m+1/2}(2n)^{n+1/2}$$
$$\times \sum_{k=-N/2}^{N/2-1}\sum_{l=-N/2}^{N/2-1} r[k,l]\left|\frac{k}{L_{\xi\eta}}\right|^m\left|\frac{l}{L_{\xi\eta}}\right|^n$$
$$\times \exp\left[-\frac{1}{2}\pi^2\delta_x^4\left(\frac{k}{L_{\xi\eta}}\right)^2\right]\exp\left[-\frac{1}{2}\pi^2\delta_y^4\left(\frac{l}{L_{\xi\eta}}\right)^2\right]$$
$$\times \exp\left(-j\frac{2\pi}{N}ki\right)\exp\left(-j\frac{2\pi}{N}lj\right)\frac{1}{L_{\xi\eta}},$$
$$\textbf{(27)}$$

where i, j are the discrete ξ, η indices.

It is clear from Eq. (25) that ξ, $\eta \geq 0$; therefore, after evaluating Eq. (27), we need only the first quadrant of the resulting $T(\xi, \eta)$ screen. To form $T(x, y)$, we must then interpolate the first quadrant of $T(\xi, \eta)$ to the full spatial (x, y) grid using the relations in Eq. (25). The last step is to multiply $T(x, y)$ by τ in Eq. (23).

Figure 3 shows an example RHNUC field realization. The RHNUC source parameters are $\sigma_x = 1.5$ mm, $\sigma_y = 1$ mm, $\delta_x = 1.25$ mm, $\delta_y = 1.1$ mm, $x_0 = 0.5$ mm, $y_0 = -0.6$ mm, $m = 2$, and $n = 1$. We used grids that were 512 points per side with an (x, y) plane spacing equal to 19.5 µm [46]. The associated (ξ, η) plane grid size and spacing were $L_{\xi\eta} = 1.18$ cm^2 and 0.23 mm^2, respectively.

Figure 4 shows the theoretical [computed using Eq. (21)] and simulated spectral densities S as well as $W(x_1, 0, x_2, 0)$. As in the previous example, the simulated moments were computed using 100,000 field realizations. Figure 4(c) shows C for the simulated S versus trial number; the inset shows C from trials 100–100,000. Overall, the agreement between simulation and theory is excellent. Note that the visually conspicuous differences between $\mathrm{Im}(W)$ theory and simulation in Figs. 4(d) and 4(e) are in fact quantitatively small. The color scale of these images is $[-0.005, 0.005]$, which is two orders of magnitude smaller than the corresponding color scale of $\mathrm{Re}(W)$.

C. Twisted Anisotropic Gaussian Schell-Model Source

For our final example, we show how to generate a twisted anisotropic Gaussian Schell-model (TAGSM) source field realization. Twisted Gaussian Schell-model (TGSM) beams were
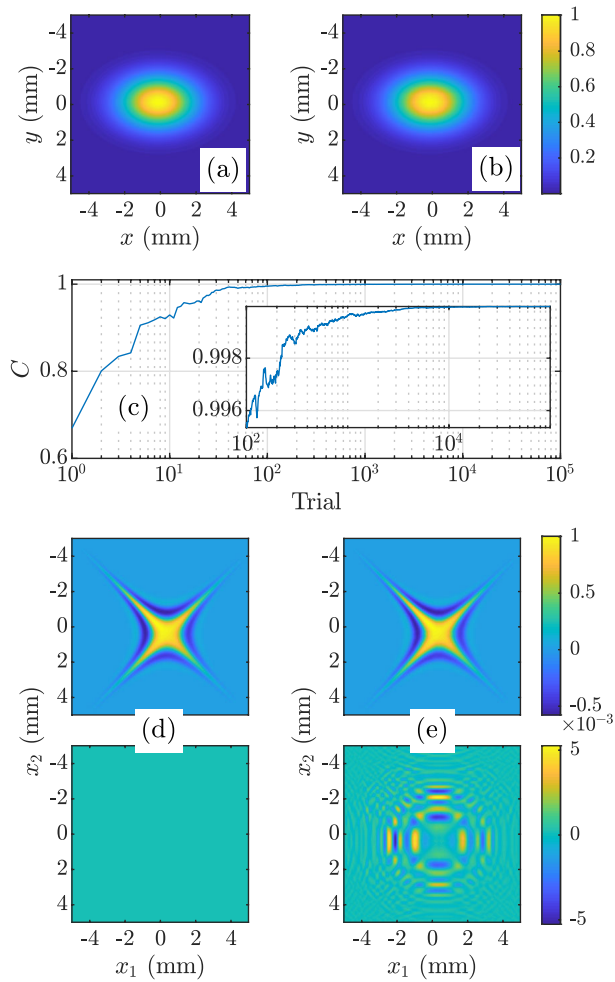
Fig. 4. RHNUC source simulation results: (a) S theory, (b) S simulation, (c) 2D correlation coefficient C for S simulation versus trial number, (d) real (top) and imaginary (bottom) parts of $W(x_1, 0, x_2, 0)$ theory, and (e) real (top) and imaginary (bottom) parts of $W(x_1, 0, x_2, 0)$ simulation.

first introduced by Simon and Mukunda [48] and were physically realized shortly thereafter [49]. Since that time, twisted beams have been extensively studied and generalized [50–54].

Despite much theoretical work, only two groups of researchers have actually realized TGSM beams, and both used a similar approach, namely, passing an anisotropic Gaussian Schell-model beam through a system of rotated cylindrical lenses [49,55]. No one, to our knowledge, has ever generated a TGSM beam using a complex transmittance screen, which in practice, can be achieved using a simple optical setup consisting of a laser, SLM, and a $4f$ spatial filter [33].

A TAGSM source has the following W:

$$W(\boldsymbol{\rho}_1, \boldsymbol{\rho}_2) = \exp\left(-\frac{x_1^2 + x_2^2}{4\sigma_x^2}\right) \exp\left[-\frac{(x_1 - x_2)^2}{2\delta_x^2}\right]$$

$$\times \exp\left(-\frac{y_1^2 + y_2^2}{4\sigma_y^2}\right) \exp\left[-\frac{(y_1 - y_2)^2}{2\delta_y^2}\right]$$

$$\times \exp\left[ju(x_1 y_2 - x_2 y_1)\right], \tag{28}$$

where u is called the twist parameter [50]. The τ, p, and h that when substituted into Eq. (2) yield the TAGSM source W are

$$\tau(\boldsymbol{\rho}) = \exp\left(-\sigma \rho^2\right),$$

$$p(\boldsymbol{v}) = \frac{\sqrt{\alpha\beta}}{\pi} \exp\left(-\alpha v_x^2\right) \exp\left(-\beta v_y^2\right),$$

$$h(\boldsymbol{\rho}, \boldsymbol{v}) = \exp\left[-j\left(x - j\alpha u y\right) v_x\right] \exp\left[-j\left(y + j\beta u x\right) v_y\right], \tag{29}$$

where α, β, and σ are

$$\frac{1}{4\sigma_x^2} = \sigma - \frac{\beta u^2}{2}, \qquad \frac{1}{2\delta_x^2} = \frac{\beta u^2}{4} + \frac{1}{4\alpha},$$

$$\frac{1}{4\sigma_y^2} = \sigma - \frac{\alpha u^2}{2}, \qquad \frac{1}{2\delta_y^2} = \frac{\alpha u^2}{4} + \frac{1}{4\beta}. \tag{30}$$

With Eq. (29), we can now produce TAGSM T using Eq. (12), namely,

$$T(\boldsymbol{\rho}) = \sqrt{2\pi}(\alpha\beta)^{1/4} \iint_{-\infty}^{\infty} r(\boldsymbol{f})$$

$$\times \exp\left[-\frac{1}{2}(2\pi)^2 \left(\alpha f_x^2 + \beta f_y^2\right)\right]$$

$$\times \exp\left(-2\pi\alpha u y f_x\right) \exp\left(2\pi\beta u x f_y\right)$$

$$\times \exp\left(-j2\pi \boldsymbol{\rho} \cdot \boldsymbol{f}\right) d^2 f. \tag{31}$$

The integrals in Eq. (31) can be evaluated using FFTs. For convenience, we express Eq. (31) in DFT form:

$$T[i, j] = \sqrt{2\pi}(\alpha\beta)^{1/4} \sum_{m=-N/2}^{N/2-1} \sum_{n=-N/2}^{N/2-1} r[m, n]$$

$$\times \exp\left[-\frac{1}{2}(2\pi)^2 \alpha \left(\frac{m}{L_x}\right)^2\right] \exp\left(-2\pi\alpha u j \frac{L_y}{N_y} \frac{m}{L_x}\right)$$

$$\times \exp\left[-\frac{1}{2}(2\pi)^2 \beta \left(\frac{n}{L_y}\right)^2\right] \exp\left(2\pi\beta u i \frac{L_x}{N_x} \frac{n}{L_y}\right)$$

$$\times \exp\left(-j\frac{2\pi}{N_x} mi\right) \exp\left(-j\frac{2\pi}{N_y} nj\right) \frac{1}{\sqrt{L_x L_y}}, \tag{32}$$

where N_x, N_y and $L_x = N_x \Delta_x$, $L_y = N_y \Delta_y$ are the x and y dimensions of the grid in points and meters (Δ_x, Δ_y are the grid spacings), respectively.

To use FFTs to compute the above matrix–vector product, we first evaluate the exponential terms containing the twist parameter u at a desired discrete x, y (i.e., i, j) location. We then compute the 2D FFT of the resulting matrix. The value of the 2D FFT at the i, j location where the twist parameter exponentials were evaluated is the true value of the screen T. We repeat this procedure for all i, j. The last step is to multiply the resulting T by the τ in Eq. (29) to form a TAGSM field realization.
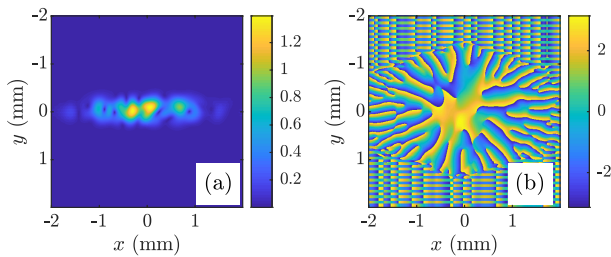
Fig. 5.　TAGSM field realization: (a) $|U|$ and (b) $\arg(U)$.
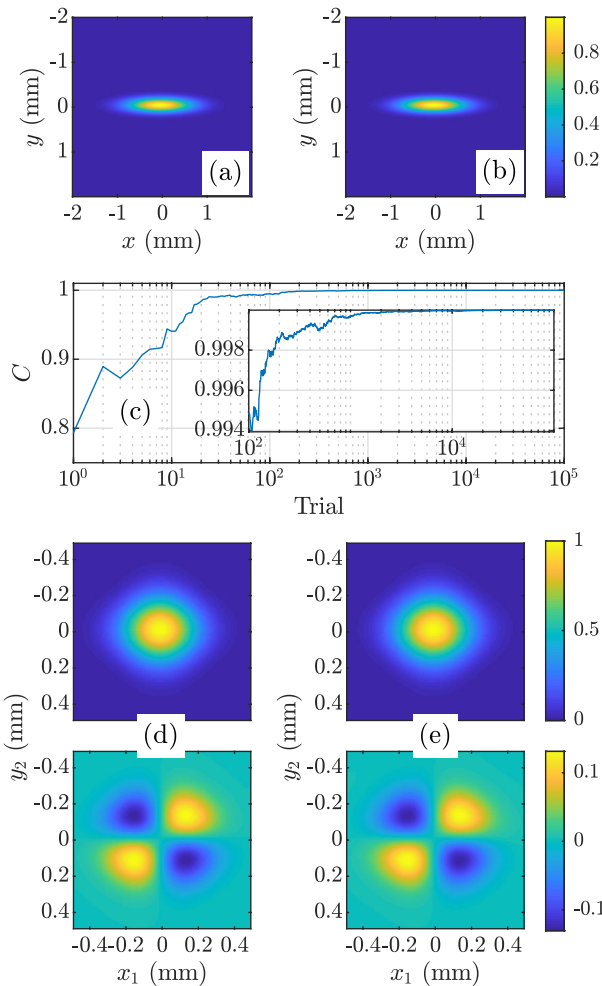

Fig. 6.　TAGSM source simulation results: (a) S theory, (b) S simulation, (c) 2D correlation coefficient C for S simulation versus trial number, (d) real (top) and imaginary (bottom) parts of $W(x_1, 0, 0, y_2)$ theory, and (e) real (top) and imaginary (bottom) parts of $W(x_1, 0, 0, y_2)$ simulation.

An example TAGSM field realization is shown in Fig. 5. The TAGSM source parameters are $\sigma = 41$ mm^{-2}, $\alpha = 0.1$ mm^2, $\beta = 0.2$ mm^2, and $u = -20$ mm^{-2}, corresponding to physical parameters $\sigma_x = 0.5$ mm, $\sigma_y = 0.11$ mm, $\delta_x = 0.15$ mm, and $\delta_y = 0.21$ mm [46].

For these proof-of-concept simulations, we used 70×70 frequency domain grids with a spacing $\Delta_f = 250$ m^{-1} [46]. Since we must evaluate the twist parameter exponentials at each i, j,

we expanded the grids to $70 \times 70 \times 4900$, where f_y (discrete index n), f_x (discrete index m), and x, y (discrete indices i, j) corresponded to dimensions 1, 2, and 3 of the grids, respectively. We then fast Fourier transformed the three-dimensional (3D) array along dimensions one and two. The mapping from the transformed 3D array $\mathcal{T}$ to T was simply

$$T[i, j] = \mathcal{T}[i, j, N(j-1) + i], \tag{33}$$

where $N = 70$ was the number of grid points. We note that by using FFTs and with $N = 70$ and $\Delta_f = 250$ m^{-1}, $\Delta_x = \Delta_y = 57.14$ μm and $L_x = L_y = 4$ mm. As a last step, we interpolated the 70×70 screens to $512 \times 512 T$ with $\Delta_x = \Delta_y = 7.81$ μm.

Figure 6 shows the theoretical [computed using Eq. (28)] and simulated S and $W(x_1, 0, 0, y_2)$. As in the previous two PCS examples, the simulated moments were computed using 100,000 field realizations. Figure 6(c) shows C for the simulated S versus trial number, and the inset shows C from trials 100–100,000. The agreement between simulation and theory is excellent, implying successful realization of the beam.

4. CONCLUSION

We presented a method to produce stochastic complex transmittance screens for synthesizing general PCSs. With the exception of a few recent papers, complex screen or phase screen methods have been used solely to synthesize Schell-model PCSs.

Here, using the genuine CSD function criterion, we derived a superposition integral to produce complex screen realizations for both uniformly (Schell-model) and non-uniformly correlated PCSs. We demonstrated and validated our method by generating, in simulation, three PCSs from the literature. Using 100,000 stochastic optical field realizations, we computed 2D slices through the corresponding 4D CSD functions. We compared the simulated results to theory and found them to be in excellent agreement.

In closing, the method presented in this paper adds to the existing literature concerning PCS synthesis. Using this approach, any PCS with a genuine CSD function can be realized using a simple optical system consisting of a laser, SLM, and $4f$ spatial filter.

REFERENCES

1. G. Gbur and T. Visser, "The structure of partially coherent fields," Prog. Opt. **55**, 285–341 (2010).
2. G. Gbur, "Partially coherent beam propagation in atmospheric turbulence," J. Opt. Soc. Am. A **31**, 2038–2045 (2014).
3. Y. Cai, Y. Chen, J. Yu, X. Liu, and L. Liu, "Generation of partially coherent beams," Prog. Opt. **62**, 157–223 (2017).
4. Y. Cai, Y. Chen, and F. Wang, "Generation and propagation of partially coherent beams with nonconventional correlation functions: a review," J. Opt. Soc. Am. A **31**, 2083–2096 (2014).

5. O. Korotkova, *Random Light Beams: Theory and Applications* (CRC Press, 2014).

6. L. Mandel and E. Wolf, *Optical Coherence and Quantum Optics* (Cambridge University, 1995).

7. J. W. Goodman, *Statistical Optics*, 2nd ed. (Wiley, 2015).

8. R. Grella, "Synthesis of generalized Collett-Wolf sources," J. Opt. **13**, 127–131 (1982).

9. P. D. Santis, F. Gori, G. Guattari, and C. Palma, "Synthesis of partially coherent fields," J. Opt. Soc. Am. A **3**, 1258–1262 (1986).

10. D. Mendlovic, G. Shabtay, and A. W. Lohmann, "Synthesis of spatial coherence," Opt. Lett. **24**, 361–363 (1999).

11. M. Santarsiero, R. Borghi, and V. Ramírez-Sánchez, "Synthesis of electromagnetic Schell-model sources," J. Opt. Soc. Am. A **26**, 1437–1443 (2009).

12. T. D. Visser, G. P. Agrawal, and P. W. Milonni, "Fourier processing with partially coherent fields," Opt. Lett. **42**, 4600–4602 (2017).

13. T. Wu, C. Liang, F. Wang, and Y. Cai, "Shaping the intensity and degree of coherence of a partially coherent beam by a 4f optical system with an amplitude filter," J. Opt. **19**, 124010 (2017).

14. M. W. Hyde, "Controlling the spatial coherence of an optical source using a spatial filter," Appl. Sci. **8**, 1465 (2018).

15. C. Pask and A. W. Snyder, "The Van Cittert-Zernike theorem for optical fibres," Opt. Commun. **9**, 95–97 (1973).

16. P. Hlubina, "Spatial and temporal coherence of light in a fibre waveguide," J. Mod. Opt. **40**, 1893–1907 (1993).

17. H. Nakano, N. Miyanaga, K. Yagi, K. Tsubakimoto, T. Kanabe, M. Nakatsuka, and S. Nakai, "Partially coherent light generated by using single and multimode optical fibers in a high-power Nd:glass laser system," Appl. Phys. Lett. **63**, 580–582 (1993).

18. A. Efimov, "Spatial coherence at the output of multimode optical fibers," Opt. Express **22**, 15577–15588 (2014).

19. A. Fathy, Y. M. Sabry, and D. A. Khalil, "Quasi-homogeneous partial coherent source modeling of multimode optical fiber output using the elementary source method," J. Opt. **19**, 105605 (2017).

20. X. Chen, J. Li, S. M. H. Rafsanjani, and O. Korotkova, "Synthesis of I_m-Bessel correlated beams via coherent modes," Opt. Lett. **43**, 3590–3593 (2018).

21. X. Zhu, F. Wang, C. Zhao, Y. Cai, and S. A. Ponomarenko, "Experimental realization of dark and antidark diffraction-free beams," Opt. Lett. **44**, 2260–2263 (2019).

22. A. Bhattacharjee, R. Sahu, and A. K. Jha, "Generation of a Gaussian Schell-model field as a mixture of its coherent modes," J. Opt. **21**, 105601 (2019).

23. R. Martínez-Herrero, P. M. Mejías, and F. Gori, "Genuine cross-spectral densities and pseudo-modal expansions," Opt. Lett. **34**, 1399–1401 (2009).

24. M. W. Hyde, IV, S. Bose-Pillai, X. Xiao, and D. G. Voelz, "A fast and efficient method for producing partially coherent sources," J. Opt. **19**, 025601 (2016).

25. M. W. Hyde, S. R. Bose-Pillai, and R. A. Wood, "Synthesis of nonuniformly correlated partially coherent sources using a deformable mirror," Appl. Phys. Lett. **111**, 101106 (2017).

26. M. W. Hyde and S. Avramov-Zamurovic, "Generating dark and antidark beams using the genuine cross-spectral density function criterion," J. Opt. Soc. Am. A **36**, 1058–1063 (2019).

27. M. W. Hyde, "Partially coherent sources generated from the incoherent sum of fields containing random-width Bessel functions," Opt. Lett. **44**, 1603–1606 (2019).

28. G. Gbur, "Simulating fields of arbitrary spatial and temporal coherence," Opt. Express **14**, 7567–7578 (2006).

29. Y. Gu and G. Gbur, "Scintillation of nonuniformly correlated beams in atmospheric turbulence," Opt. Lett. **38**, 1395–1397 (2013).

30. T. Shirai, O. Korotkova, and E. Wolf, "A method of generating electromagnetic Gaussian Schell-model beams," J. Opt. A **7**, 232–237 (2005).

31. X. Xiao and D. Voelz, "Wave optics simulation approach for partial spatially coherent beams," Opt. Express **14**, 6986–6992 (2006).

32. D. Voelz, X. Xiao, and O. Korotkova, "Numerical modeling of Schell-model beams with arbitrary far-field patterns," Opt. Lett. **40**, 352–355 (2015).

33. M. W. Hyde, S. Basu, D. G. Voelz, and X. Xiao, "Experimentally generating any desired partially coherent Schell-model source using phase-only control," J. Appl. Phys. **118**, 093102 (2015).

34. M. W. Hyde, S. Bose-Pillai, D. G. Voelz, and X. Xiao, "Generation of vector partially coherent optical sources using phase-only spatial light modulators," Phys. Rev. Appl. **6**, 064030 (2016).

35. M. W. Hyde, IV, S. Basu, D. G. Voelz, and X. Xiao, "Generating partially coherent Schell-model sources using a modified phase screen approach," Opt. Eng. **54**, 120501 (2015).

36. H. T. Yura and S. G. Hanson, "Digital simulation of an arbitrary stationary stochastic process by spectral representation," J. Opt. Soc. Am. A **28**, 675–685 (2011).

37. C. A. Mack, "Generating random rough edges, surfaces, and volumes," Appl. Opt. **52**, 1472–1480 (2013).

38. M. W. Hyde, "Generating electromagnetic Schell-model sources using complex screens with spatially varying auto- and cross-correlation functions," Results Phys. **15**, 102663 (2019).

39. X. Xiao and D. Voelz, "Numerical implementation of a spatially varying correlation beam: turbulence propagation example," in *Imaging and Applied Optics* (OSA, 2017), paper PTu1D.3.

40. M. W. Hyde, X. Xiao, and D. G. Voelz, "Generating electromagnetic nonuniformly correlated beams," Opt. Lett. **44**, 5719–5722 (2019).

41. D. S. Watkins, *Fundamentals of Matrix Computations*, 2nd ed. (Wiley, 2002).

42. F. Gori and M. Santarsiero, "Devising genuine spatial correlation functions," Opt. Lett. **32**, 3531–3533 (2007).

43. A. Efimov, "Gigabit per second modulation and transmission of a partially coherent beam through laboratory turbulence," Proc. SPIE **9739**, 97390L (2016).

44. A. Efimov, "Effects of residual coherence on the scintillation of a partially coherent beam," Opt. Express **27**, 26874–26881 (2019).

45. S. A. Ponomarenko, "A class of partially coherent beams carrying optical vortices," J. Opt. Soc. Am. A **18**, 150–156 (2001).

46. M. Hyde, "MATLAB R2018b generalized complex screen simulation code," figshare, 2019, https://doi.org/10.6084/m9.figshare.10058318, retrieved 27 Oct 2019.

47. J. Yu, Y. Cai, and G. Gbur, "Rectangular Hermite non-uniformly correlated beams and its propagation properties," Opt. Express **26**, 27894–27906 (2018).

48. R. Simon and N. Mukunda, "Twisted Gaussian Schell-model beams," J. Opt. Soc. Am. A **10**, 95–109 (1993).

49. A. T. Friberg, E. Tervonen, and J. Turunen, "Interpretation and experimental demonstration of twisted Gaussian Schell-model beams," J. Opt. Soc. Am. A **11**, 1818–1826 (1994).

50. Z. Mei and O. Korotkova, "Random sources for rotating spectral densities," Opt. Lett. **42**, 255–258 (2017).

51. R. Borghi, "Twisting partially coherent light," Opt. Lett. **43**, 1627–1630 (2018).

52. F. Gori and M. Santarsiero, "Devising genuine twisted cross-spectral densities," Opt. Lett. **43**, 595–598 (2018).

53. M. Santarsiero, F. Gori, and M. Alonzo, "Higher-order twisted/astigmatic Gaussian Schell-model cross-spectral densities and their separability features," Opt. Express **27**, 8554–8565 (2019).

54. C. S. D. Stahl and G. Gbur, "Twisted vortex Gaussian Schell-model beams," J. Opt. Soc. Am. A **35**, 1899–1906 (2018).

55. H. Wang, X. Peng, L. Liu, F. Wang, Y. Cai, and S. A. Ponomarenko, "Generating bona fide twisted Gaussian Schell-model beams," Opt. Lett. **44**, 3709–3712 (2019).